A viscoplastic approach to corium spreading during a severe nuclear accident

Thomas Schiano, Barbara Bigot, Jean-François Haquet, Pierre Saramito, Claude Smutek

A viscoplastic approach to corium spreading during a severe nuclear accident

Thomas Schiano[a,b,*], Barbara Bigot[a], Jean-François Haquet[a], Pierre Saramito[b], Claude Smutek[c]

[a] *CEA, DES, IRESNE, DTN, SMTA, LMAG, Cadarache F-13108 St Paul Lez Durance France*

[b] *Laboratoire Jean Kuntzmann, Grenoble-Alpes University, 700 Avenue Centrale, 38400 Saint Martin d'Hères*

[c] *Laboratoire GéoSciences Réunion, Réunion University, Institut de Physique du Globe de Paris, Sorbonne Paris-Cité, 15 av. René Cassin, 97400 Saint-Denis*

Abstract

A viscoplastic model for lava is presented, and its use for corium spreading is argued with dimensionless numbers. It describes the tridimensional flow as non-Newtonian and non-isothermal. Using an adaptive finite element method based on C++ library Rheolef, simulations are ran and compared to the VEU7 corium spreading test. A sensitivity analysis on the viscoplastic parameters of corium that are not well-known is conducted. Tridimensional solution of the problem is computed from the bidimensional height-averaged solution.

Keywords: Spreading, Corium, Lava, Severe accidents, Simulation

1. Introduction

During a nuclear reactor severe accident such as those of Three Mile Island, Chernobyl or Fukushima, it is crucial to contain the radiological consequences to the power plant. A severe accident of a Pressurized Water Reactor (PWR) occurs when the nuclear fuel, in case of loss of cooling, melts and mixes with the core structures (assemblies and internal structures) to form a magma so-called corium (mixture of oxides and metals at 3000K). Several strategies are studied to cool the corium and to limit its propagation in the reactor plant in order to avoid the outside contamination: the In-Vessel Retention (IVR) whose purpose is to contain and cool the corium in the vessel lower head; and the Ex-Vessel Retention (EVR) whose purpose is to spread the corium on the basemat to promote its cooling and prevent basemat ablation by increasing the corium cooling surface and thus reducing the thermal load on the reactor structure. End of spreading serves as the initial condition of the subsequent EVR part, called the Molten Core-Concrete Interaction (MCCI) [1]. This paper focuses on the EVR strategy dedicated to the corium spreading. Understanding the corium spreading is a crucial issue for mitigation strategies in future reactors to assess the consequences of a severe accident during the propagation of corium and to implement efficient solutions of corium cooling before the integrity of the containment barrier is threatened. In 90's, the EVR strategy was integrated into the design of European Pressurized Reactor (EPR) in which a core-catcher concept is dedicated to the spreading of the melt on a concrete basemat [2]. In this context, in early 2000s, prototypic corium spreading experiments such as the VULCANO tests [1]

*This is to indicate the corresponding author.
Email address: thomas.schiano@cea.fr (Thomas Schiano)

and subsequent benchmark on the VEU7 test [3] provide valuable experimental data for a laminar regime corresponding to the end of the spreading. More recently, the VEU9 test in the same facility yielded more insight on the use of sacrificial material on spreading sections [4, 5]. These data tests allow evaluating the safety codes. Current industrial corium spreading codes including THEMA [6] and MELTSPREAD [7] describe the corium as a Newtonian fluid with the finite difference method as spatial discretization or CORFLOW [8] using a regularized viscoplastic Binghamian description of the fluid through the finite volume method. More recently, MELTSPREAD-CORQUENCH [9] as shown capabilities to describe debris cooling by water ingression, crust anchoring and melt eruption mechanisms during spreading, and a new Moving Particle Semi-implicit (MPS) method has been proposed by Yamaji et al. [10] for MCCI in severe accidents.

High density and temperature fluid spreading is an issue met in many situations such as volcanic lava flows and nuclear severe accidents. These are described by complex multiphase flows characterized by coupled multi-physics phenomena such as solidification due to heat transfers (at the surface by radiation or by convection in the presence of water, with the substrate by conduction), the rheology of the fluid (possibly non Newtonian) or interactions with the substrate (ablation, degassing). A viscoplastic (non Newtonian) description of corium has been gathering interest since the viscosity and yield stress measurements made by Roche et al. [11]. The presence of a solid fraction in corium due to its non eutectic properties lead us to consider a greater range of fluid behavior. Fig. 1 presents the stress tensor according to the deformation rate tensor and allows illustrating the different behaviors of a fluid according to the Herschel-Bulkley [12] viscoplastic model that depends on two parameters: the fluid index, n, and yield stress, τ_y. For $n = 1$ and $\tau_y = 0$, this fluid is considered as Newtonian, for $n = 1$ and $\tau_y \neq 0$ as viscoplastic Binghamian [13], and for $n \neq 1$ and $\tau_y \neq 0$ as general viscoplastic.

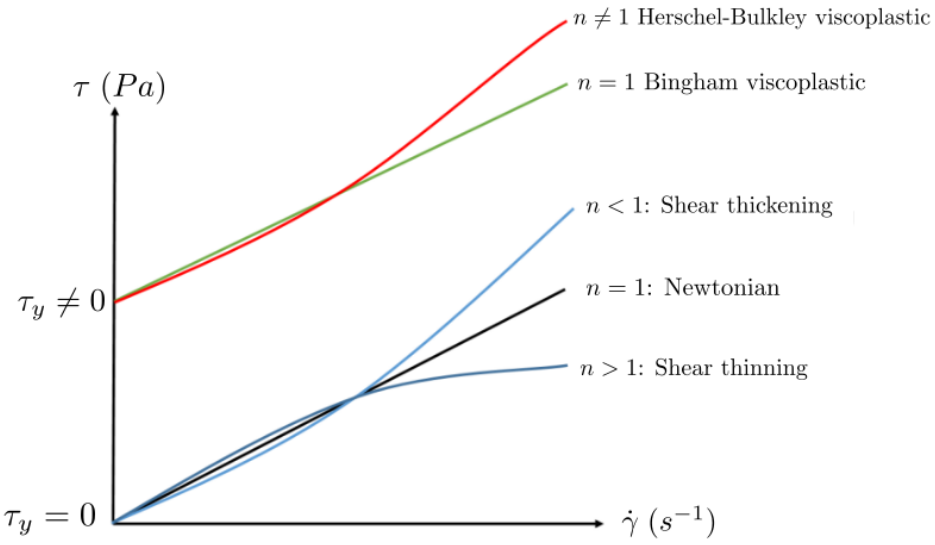

Figure 1: Stress tensor according to deformation rate tensor illustrating the different behaviors of a fluid according to the Herschel-Bulkley model with two parameters: the fluid index, n, and yield stress, τ_y. For $n = 1$ and $\tau_y = 0$, fluid is considered as Newtonian, for $n = 1$ and $\tau_y \neq 0$ as Binghamian, and for $n \neq 1$ as viscoplastic.

As pointed out by Saramito and Wachs [14], the regularization approach currently used in industrial codes lacks a general convergence result of the solution with the regularization parameter and cannot follow the unyielded regions of a yield stress fluid flow with the deformation rate tensor $\dot{\boldsymbol{\gamma}} =$

0. Recently, Bernabeu et al. [15, 16] derived a new unregularizated model for the lava flows using shallow-depth approximation for tridimensional cooling of viscoplastic fluid with a bidimensional height-averaged finite element approach and the simulations were successfully compared to lava flows. Here, we propose to adapt this viscoplastic model to the corium spreading with a second-order temperature polynomial approximation with non-constant viscosity using a model based on Shaw law [17]. A comparison between lava and corium flow regime through similarity criteria and simulations of the VEU7 test are then presented. A sensitivity analysis for Shaw model parameter, fluid index and yield stress of the Herschel-Bulkley viscoplastic model is also performed. Tridimensional velocity and temperature fields are reconstructed from the bidimensional height-averaged solution, substrate temperature is also calculated and compared to the experimental measurements. Finally, we discuss about results.

2. Mathematical model

In this section, we present the viscoplastic model. Fig. 2 shows the spreading scheme with the melt spread. It involves three domains, denoted by the indices f,s that represent respectively the melt, the substrate and the ambient environment of the spread. Let Q be an open set of $\mathbb{R}^3$ of regular border ∂Q be the whole domain. It splits as $Q = Q_f(t) \cup Q_s$ where $Q_f(t)$ is the melt flow region, and Q_s the substrate. The boundary of the melt flow region also splits as $\partial Q_f(t) = \Gamma_f(t) \cup \Gamma_s \cup \Gamma_w$ where $\Gamma_f(t)$ is the free surface of the flow, Γ_s the horizontal plane where the melt is in contact with the substrate and Γ_w the vertical walls. Finally, a part $\Gamma_e \subset \Gamma_s$ corresponds to the alimentation region, where there is an inflow.

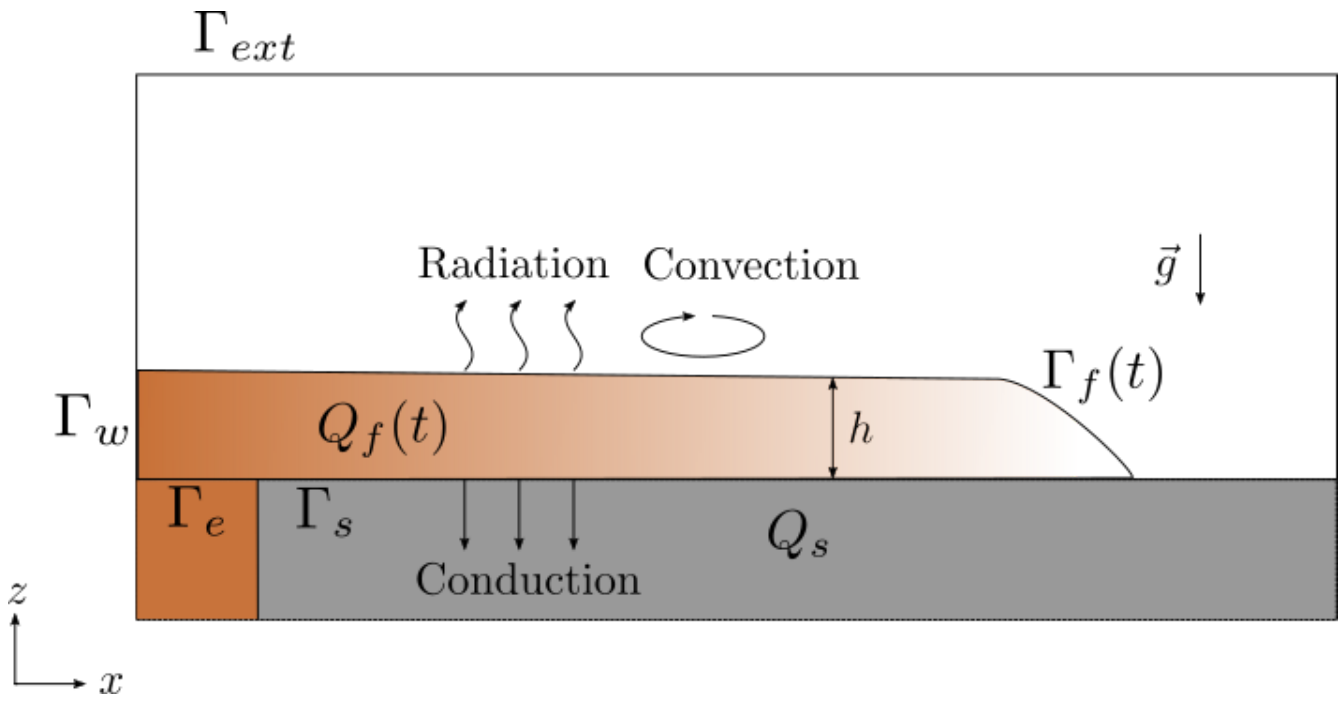

Figure 2: Corium spreading: its geometry and notations.

2.1. Tridimensional model

The Herschel-Bulkley model expresses the deviatoric part $\boldsymbol{\tau}$ of the Cauchy stress tensor in the melt as

$$\begin{cases} \boldsymbol{\tau} = \left(K(\theta)\dot{\boldsymbol{\gamma}}^{n-1} + \dfrac{\tau_y(\theta)}{|\dot{\boldsymbol{\gamma}}|} \right) \dot{\boldsymbol{\gamma}} & \text{when } \dot{\boldsymbol{\gamma}} \neq 0, \\ |\boldsymbol{\tau}| \leq \tau_y(\theta) & \text{otherwise,} \end{cases} \tag{1a}$$

where $\dot{\boldsymbol{\gamma}} = \nabla \boldsymbol{u} + \nabla \boldsymbol{u}^T$ is the shear rate tensor, $\boldsymbol{u}$ is the velocity and θ is the temperature. Also $K(\theta)$ is the temperature-dependent consistency, $\tau_y(\theta)$, the temperature-dependent yield stress and n is the power-law index, As depicted on fig. 1, for $\tau_y = 0$ and $n = 1$, the fluid is Newtonian, and $K(\theta)$ is the temperature-dependent consistency index. Here, the temperature dependence of both consistency index and yield stress follow the Shaw model with the same coefficient [17] :

$$K(\theta) = K_e \exp\left(Arr \left(\frac{\theta_e - \theta}{\theta_e - \theta_a} \right) \right)$$
$$\tau_y(\theta) = \tau_{y,e} \exp\left(Arr \left(\frac{\theta_e - \theta}{\theta_e - \theta_a} \right) \right)$$

with K_e and $\tau_{y,e}$, the value of $K(\theta)$ and $\tau_y(\theta)$ at the inlet reference temperature θ_e. The values of the constants $\tau_{y,e}$, K_e and Arr are determined through the viscosity and yield stress measurements of Roche et al. [11] and Ramacciotti et al. [18]. Assuming a constant density ρ, the mass conservation equation in the melt reduces to

$$\nabla . \boldsymbol{u} = 0 \tag{1b}$$

while the momentum conservation equation in the melt reads:

$$\rho(\partial_t \boldsymbol{u} + (\boldsymbol{u}.\nabla)\boldsymbol{u}) - \nabla . \boldsymbol{\tau} + \nabla p = \rho \boldsymbol{g} \tag{1c}$$

where p is the pressure. Conversely, the energy conservation equation in the melt expresses:

$$\rho c_p(\partial_t \theta + \boldsymbol{u}.\nabla\theta) - \nabla.(k\nabla\theta) = \boldsymbol{\tau} : \dot{\boldsymbol{\gamma}} \tag{1d}$$

where c_p is the specific heat capacity of the melt and k, its the heat conduction coefficient. Note the friction dissipation term $\boldsymbol{\tau} : \dot{\boldsymbol{\gamma}}$ in the right-hand-side. Assuming that the substrate Q_s behaves as a rigid solid, the energy conservation equation in the substrate is:

$$\rho_s c_{ps} \partial_t \theta - \nabla.(k_s \nabla\theta) = 0 \tag{1e}$$

where ρ_s is the density of the substrate, c_{ps}, its specific heat capacity, and k_s, its heat conduction coefficient. The set of equations (1a)-(1e) is closed by initial and boundary conditions. First, assume that the free surface $\Gamma_f(t)$ could explicitly be described by the melt height function h such that

$$\Gamma_f(t) = \left\{ (x, y, z) \in \mathbb{R}^3 \ ; \ z = h(t, x, y) \right\}$$

where, by convention, the plane $z = 0$ coincides with the melt-substrate interface Γ_s, see fig. 2. Note that the height $h(t, x, y)$ is defined for all $t > 0$ and $(x, y) \in \Gamma_s$. Then, the transport of the free surface by the flow writes:

$$\partial_t h + u_x \partial_x h + u_y \partial_y h - u_z = 0 \tag{1f}$$

The initial conditions velocity, height and temperature are:

$$\boldsymbol{u}(t=0) = \boldsymbol{u}_0 \text{ in } Q_f(t=0) \tag{1g}$$
$$\theta(t=0) = \theta_0 \text{ in } Q_f(t=0) \cup \Gamma_s \cup Q_s \tag{1h}$$
$$h(t=0) = h_0 \text{ on } \Gamma_s \tag{1i}$$

where $\boldsymbol{u}_0$, θ_0 and h_0 are known from experimental measurements. It corresponds to $h_0 = 0$, $\boldsymbol{u}_0 = 0$ and $\theta_0 = \theta_a$, the atmospheric temperature. A Dirichlet condition for velocity on the substrate plane Γ_s is considered, as they are considered as no-slip boundaries. It is completed with the inlet velocity condition for the z-component:

$$u_x = u_y = 0 \text{ and } u_z = w_e \text{ on } \Gamma_s \cap \partial Q_f(t) \tag{1j}$$

where w_e is the inlet velocity, which is deduced from the measured flow rate. On the vertical walls Γ_w, the no-slip boundary condition simply becomes $\boldsymbol{u} = 0$. On the free surface $\Gamma_f(t)$, surface tension effects are neglected, so the normal Cauchy stress is just zero, i.e.:

$$(\boldsymbol{\tau} - p\boldsymbol{I}).\boldsymbol{n} = 0 \text{ on } \Gamma_f(t) \tag{1k}$$

where $\boldsymbol{n}$ denotes the outward unit normal at $Q_f(t)$ on the free surface $\Gamma_f(t)$. A Dirichlet condition for temperature on Γ_s is given to model inlet temperature in its inlet region Γ_e:

$$\theta = \theta_e \text{ on } \Gamma_s \cap \Gamma_e \tag{1l}$$

On Γ_s but outside of this inlet region Γ_e, the melt is in contact with the substrate: the temperature is continuous across Γ_s while the heat transfer is considered to be mostly conductive:

$$\theta_{|Q_f} = \theta_{|Q_s} \text{ on } \Gamma_s \backslash \Gamma_e \tag{1m}$$
$$k\,\boldsymbol{n}.\nabla(\theta_{|Q_f}) = k_s \boldsymbol{n}.\nabla(\theta_{|Q_s}) \text{ on } \Gamma_s \backslash \Gamma_e \tag{1n}$$

where $\theta_{|Q_f}$ (resp. $\theta_{|Q_s}$) denotes the restriction of the temperature θ in the melt (resp. substrate) region and $\boldsymbol{n}$ is the outward unit normal at $Q_f(t)$ on the substate plane Γ_s. On the free surface $\Gamma_f(t)$, both radiative and convective heat transfers with the environment are considered:

$$k\,\boldsymbol{n}.\nabla\theta + \epsilon\sigma_{SB}\left(\theta^4 - \theta_a^4\right) + \lambda(\theta - \theta_a) = 0 \text{ on } \Gamma_f(t) \tag{1o}$$

where ϵ is the emissivity, σ_{SB}, the Stefan-Boltzmann constant and λ, the convective heat transfer coefficient. Finally, the temperature at the bottom of the substrate is assumed to tend o the atmospheric one:

$$\theta(z=-\infty) = \theta_a. \tag{1p}$$

The set of equations (1a)-(1p) defines the tridimentional viscoplastic melt spreading problem with four unknowns $(\boldsymbol{\tau}, \boldsymbol{u}, p, h)$ that depends both upon time and space, while the computational space is time-dependent since it involves a free-surface.

2.2. Bidimensional reduced model

In 2013, Bernabeu et al. [15] showed that the tridimensional isothermal viscoplastic free-surface problem could be reduced as a bidimensional one in terms of the height h only as unkown. This reduction bases on an asymptotic analysis, assuming that the aspect ratio of the heigh versus the

horizontal length is small. In 2016, Bernabeu et al. [16] extended this result to non-isothermal viscoplastic free-surface flows. In that case, all the unknowns of the tridimensional problem express explicitly in terms of only the height h and the vertical-averaged temperature $\overline{\theta}$. The notation $\overline{\xi}$ represents the vertical-averaged value of a quantity, defined for all ξ by

$$\overline{\xi}(t,x,y) = \begin{cases} \dfrac{1}{h(t,x,y)} \displaystyle\int_0^{h(t,x,y)} \xi(t,x,y,z)\mathrm{d}z & \text{when } h(t,x,y) \neq 0 \\ 0 \text{ otherwise} \end{cases}$$

we obtain the following formulation from Bernabeu et al. [16], the tridimensional problem (1a)-(1p) reduces to find $(h, \overline{\theta})$ defined on Γ_s such that the height h satisfies

$$\begin{cases} \partial_t h - \nabla_\parallel . \big(\mu(h,\overline{\theta})\, \nabla_\parallel h\big) = w_e \text{ in }]0,T[\times\Omega & \text{(2a)} \\ h(t=0) = h_0 \text{ in } \Omega & \text{(2b)} \\ \boldsymbol{n}.\nabla_\parallel h = 0 \text{ on }]0,T[\times\partial\Omega, & \text{(2c)} \end{cases}$$

where $\Omega \subset \Gamma_s$ denotes the bidimensional bounded computational domain, $T > 0$ is the final time of computation and $\boldsymbol{n}$ is the outward unit normal on its boundary in the horizontal plane. Also, for convenience, the notation $\nabla_\parallel = (\partial_x, \partial_y)$ is introduced. The μ diffusion coefficient in the previous parabolic equation (2a) is given by:

$$\mu(h,\overline{\theta}) = \begin{cases} \dfrac{n\left\{(n+1)\rho g h|\nabla_\parallel h| + n\tau_y(\overline{\theta})\right\}\left\{\rho g h|\nabla_\parallel h| - \tau_y(\overline{\theta})\right\}^{1+\frac{1}{n}}}{(n+1)\,(2n+1)\,(\rho g)^2\,|\nabla_\parallel h|^3\,K(\overline{\theta})^{\frac{1}{n}}} & \text{when } \rho g h|\nabla_\parallel h| > \tau_y(\overline{\theta}) \\ 0 \quad \text{otherwise} \end{cases}$$

Note that the consistency $K(\overline{\theta})$ and the yield stress $\tau_y(\overline{\theta})$ involves now the vertical-averaged temperature $\overline{\theta}$. Also, for a Newtonian fluid, i.e. $n = 1$ and $\tau_y = 0$, we observe that $\mu = \rho g h^3/(3K)$ and then (2a) reduces to the usual lubrication equation for a Newtonian fluid, as expected. In the general case, the solution h depends upon the vertical-averaged temperature $\overline{\theta}$, which is provided by a coupled equation.

The tridimensional energy conservation (1d) in the melt is also reduced to a bidimensional one by introducing a closure shape function φ, which is a second order polynomial that satisfies $\overline{\varphi} = 1$, such that $\theta(t,x,y,z) = \varphi(t,x,y,z)\,\overline{\theta}(t,x,y)$. Then, $\overline{\theta}$ satisfies also a bidimensional evolution equation, see Bernabeu et al. [16], appendix A for details.

Bernabeu et al. [16] have shown that no significant improvement in terms on temperature distribution is gained from using a third order polynomial distribution function φ over a second order one. We thus use the former here, with $\varphi = az^2 + bz + c$, and neglect the $\nabla_\parallel.\big(h\left(\overline{\varphi\boldsymbol{u}}_\parallel - \overline{\boldsymbol{u}}_\parallel\right)\big)$ term by taking $\overline{\varphi u_\parallel} = \overline{u_\parallel}$. The energy conservation (1d) together with its associated boundary and initial conditions become:

$$\begin{cases} h\big(\partial_t\overline{\theta} + \overline{\varphi\boldsymbol{u}}_\parallel.\nabla_\parallel\overline{\theta}\big) + \left(-\dfrac{2ah}{\rho c_p/k}\right)\overline{\theta} \\ \qquad = w_e(\theta_e - \overline{\theta})\mathbb{I}_{\Gamma_e} \text{ in }]0,T[\times\Omega & \text{(3a)} \\ \overline{\theta}(t=0) = \theta_a \text{ in } \Omega & \text{(3b)} \\ \boldsymbol{n}.\nabla_\parallel\overline{\theta} = 0 \text{ on }]0,T[\times\partial\Omega & \text{(3c)} \end{cases}$$

with $\mathbb{I}_{\Gamma_e}$ the indicator function for the alimentation region and

$$\begin{cases} \partial_z \varphi + \left(\dfrac{\epsilon \sigma_{SB} (\theta_e - \theta_a)^3}{k} p_\psi(\overline{\theta}\varphi) + \dfrac{\lambda}{k} \right) \varphi = 0 \text{ on }]0; +\infty[\times \partial\Omega_f(t) & \text{(4a)} \\ -\partial_z \varphi + \dfrac{k_s}{k} \left(\dfrac{\rho c_p}{k\, \pi t} \right)^{1/2} \varphi = 0 \text{ on }]0; +\infty[\times \Gamma_s & \text{(4b)} \end{cases}$$

with $p_\psi(\overline{\theta}\varphi) = (\overline{\theta}\varphi)^3 + 4\psi(\overline{\theta}\varphi)^2 + 6\psi^2(\overline{\theta}\varphi) + 4\psi^3$, $\psi = \frac{\theta_a}{\theta_e - \theta_a}$, used in order to linearise the radiation term and $\overline{\boldsymbol{u}}_\parallel$ the vertical-averaged velocity along the x-axis and the y-axis:

$$\overline{\mathbf{u}}_\parallel = \begin{cases} -\dfrac{n \left\{ (n+1)\rho g h |\nabla_\parallel h| + n\tau_y(\overline{\theta}) \right\} \left\{ \rho g h |\nabla_\parallel h| - \tau_y(\overline{\theta}) \right\}^{1+\frac{1}{n}}}{(n+1)\,(2n+1)\; h\; (\rho g)^2\; |\nabla_\parallel h|^3\; K(\overline{\theta})^{\frac{1}{n}}} \nabla_\parallel(h) & \text{when } \rho g h |\nabla_\parallel h| > \tau_y(\overline{\theta}) \\ 0 \quad \text{otherwise} \end{cases}$$

2.3. Numerical resolution in the melt

The nonlinear reduced bidimensional problem in $(h, \overline{\theta})$ is discretized using a second-order backward finite difference scheme in time (BDF2), see Bernabeu et al. [16]. The resulting sequence of nonlinear problems are solved using an under-relaxed fixed point algorithm. These equations are discretized spatially using an adaptive finite element method based on the procedure introduced by Roquet and Saramito [19] using the Rheolef C++ library [20] and the bamg mesh generator [21]. At each time step, the mesh is adapted to follow the front by using the height h as an adaptation criterion, since it shows sharp gradients at this location, resulting in fig. 3.

Once the solution $(h, \overline{\theta})$ of the reduced problem has been solved numerically. The tridimensional solution $(\boldsymbol{\tau}, \boldsymbol{u}, p)$ of the initial problem in the melt Ω_f is then obtained from explicit expressions as a post-treatment, see Bernabeu et al. [16].

2.4. Explicit expression in the substrate

The temperature θ in the substrate could also be deduced from explicit expressions. Indeed, following to Carslaw and Jaeger [22, p. 58-64], the time-discretized solution to a conduction problem such as (1e) in a semi-infinite domain writes for all $(x, y) \in \Omega$ and $z < 0$:

$$\begin{aligned} \theta(t_n, x, y, z) = \theta_a + \sum_{k=1}^{n} (\theta(t_k, x, y, 0) - \theta_a) \Bigg[\mathbb{I}_{]t_{k-1}, t_k[}(t_n) \left\{ 1 - \operatorname{erf}\left(\frac{z}{2\sqrt{\alpha(t_n - t_{k-1})}} \right) \right\} \\ + \; \mathbb{I}_{]t_k, +\infty[}(t_n) \left\{ \operatorname{erf}\left(\frac{z}{2\sqrt{\alpha(t_n - t_k)}} \right) - \operatorname{erf}\left(\frac{z}{2\sqrt{\alpha(t_n - t_{k-1})}} \right) \right\} \Bigg] \end{aligned} \quad (5)$$

where $\alpha = k_s/(\rho_s c_{ps})$ the thermal diffusivity and $\mathbb{I}_S(\xi)$ denotes the indicator function, which is one when its argument ξ belongs to the set S and zero otherwise. Also, $\theta(t_k, x, y, 0)$ denotes the temperature at the interface between the melt and the substrate, which is known from the previous computation. Description of the temperature field in the substrate is of major importance in the case of severe accidents, as it yields information on the integrity of the power plant.

3. Comparison between lava and corium

The preceding dimensional conservation equations and their boundary conditions give rise to a set of dimensionless number. The values of the material and geometrical properties are given in tables 1 and 2, taken from the 2010 Piton de la Fournaise measurements and lava studies [17, 23, 24, 25, 26] for lava and from general corium material investigations and the VEU7 test [1, 3, 8, 11, 18, 27, 28, 29] for corium. Using those properties, the dimensionless numbers for both materials and experiments are computed and compared in table 3. The properties are taken at initial temperature θ_e for lava and corium, respectively 1423 K and 2450 K. We take the characteristic velocity $U = \left(\frac{\rho g H^2}{K_e L}\right)^{1/n} H$.

Table 1: Flow properties of the Piton de la Fournaise lava eruption [17, 23, 24, 25, 26] and of the VEU7 corium spreading test [1, 3, 8, 11, 18, 27, 28, 29].

Quantity	Symbol	Lava	Corium
Characteristic height m	H	1	$6.5\ 10^{-2}$
Characteristic length m	L	10^3	$4.0\ 10^{-1}$
Aspect ratio	$\varepsilon = \frac{H}{L}$	10^{-3}	0.15
Characteristic velocity $m.s^{-1}$	U	$2.16\ 10^{-3}$	1.53
Inlet fluid temperature K	θ_e	1423	2450
Initial substrate and air temperature K	θ_a	303	303

Table 2: Material properties of the Piton de la Fournaise lava eruption [17, 23, 24, 25, 26] and of the VEU7 corium spreading test [1, 3, 8, 11, 18, 27, 28, 29].

Quantity	Symbol	Lava	Corium
Spread density $(kg.m^{-3})$	ρ	2200	5100
Air density $(kg.m^{-3})$	ρ_a	1.2	1.2
Dynamic viscosity at temperature θ_e $(Pa.s)$	K_e	10^4	$2.24\ 10^1$
Yield stress at temperature θ_e (Pa)	$\tau_{y,e}$	10^2	10^2
Emissivity $(-)$	ϵ	0.95	0.8
Thermal conductivity $(W.m^{-1}.K^{-1})$	k	2	3
Specific heat $(J.kg^{-1}.K^{-1})$	c_p	1225	995.6
Convective heat transfer coefficient with air $(W.m^{-2}.K^{-1})$	λ	80	300

Table 3: Dimensionless numbers, computed using the data from table 1 and table 2.

Similarity criterion	Lava	Corium
Reynolds number: $Re = \frac{\rho U L}{K_e}$	$4.75\ 10^{-1}$	$1.40\ 10^2$
Bingham number: $Bi = \frac{\tau_{y,e} L}{K_e U}$	4.630	$1.890\ 10^{-1}$
Péclet number: $Pe = \frac{\rho c_p U L}{k}$	$2.91\ 10^6$	$1.69\ 10^5$
Brinkman number: $Br = \frac{U^2 K_e}{k(\theta_e - \theta_a)}$	$2.08\ 10^{-5}$	$1.25\ 10^{-2}$
Stanton number: $St = \frac{\lambda}{\rho U c_p} = \frac{Nu}{Pe}$	$1.37\ 10^{-5}$	$1.85\ 10^{-4}$
Radiation number: $R = \frac{\epsilon \sigma_{SB} (\theta_e - \theta_a)^3 L}{k}$	$3.78\ 10^1$	$2.70\ 10^1$

The values of the Péclet number Pe between lava and corium flows are of the same order of magnitude, with high values indicating that heat transfer in the bulk is mainly advective for both

cases. The Stanton number St replaces the Nusselt number as the latter is not a similarity criterion. Its relatively low value compared to the radiation number R informs us that at the free surface, the heat transfer is predominantly radiative in nature. In the case of underwater spreading, that may not be true.

In the case of both lava and corium spreading, the Reynolds number indicates that the flow is laminar, though inertial forces are two orders of magnitudes greater in the latter case. However, the VEU7 spreading test does not have the same scales of an hypothetical spreading process in the case of a nuclear severe accident, notably in terms of length and velocity. In that configuration, the flow regime would probably be turbulent with high values of the Reynolds number.

The Brinkman number is three orders of magnitude higher for corium than for lava, indicating a higher influence on the system's energy variation from the shear stress, it remains low enough to be negligible.

The Bingham number for corium is lower than for lava, though it uses properties at a higher temperature. Using the model developed by Rammaciotti et al. [18] for dynamic viscosity and Ancey and Jorrot [30] for the yield stress, we obtain a Bingham number of 2 for a corium at 1500 K, a temperature close to that of lava.

Though the order of magnitude differ for some of these similarity criteria, they stay in the same regime range hence we expect the behavior of corium spreading to be sensibly similar to that of lava, justifying the use of a viscoplastic model for corium spreading, though it is necessary to know the temperature evolution during the spreading to judge if this comparison is relevant.

The computation of characteristic times completes this dimensional analysis : the inertial, viscous and hydrostatic characteristic times, respectively $t_{inertia} = \frac{L}{U} = 0.26s$, $t_{viscosity} = \frac{H^2\rho}{K_e} = 0.96s$ and $t_{hydrostatic} = \frac{LU}{gH} = 0.96s$ are of the same order, while the characteristic time for thermal diffusion $t_{thermal} = \frac{H^2\rho c_p}{k} = 7150s$ is 4 orders of magnitude greater. The timescale of the VEU7 test is $\sim 10s$, thus we expect only minor influence of temperature change in the conservation equations of the spreading, though it may change physical properties through the use of the Shaw model.

This dimensional analysis coupled with our subsequent use of self-similar solutions shows that the dominant balance in the VEU7 spreading experiment is the gravity-viscosity one.

4. Experimental facilities

Experiments to study prototypical corium spreading have been conducted in facilities such as FARO [31] and VULCANO [1]. The VEU7 experiment has been performed in the latter. It consists in the melting of corium using plasma torches, its pouring in a stabilization pool, then its spreading on a test section constituted of two channels with two different substrates, a concrete one and a ceramic one, as depicted on figs. 4 and 5. In our simulation, the two channels geometry is represented, as well as the stabilization pool as shown on fig. 5. The inlet velocity condition is computed from the constant mass flow rate of 4.3 kg/s for a duration of 7.7 s according to [3]. It is implemented in the code so that the inlet velocity at the borders of the stabilization pool is null using a first order polynomial distribution such that its integral over the inlet domain is equal to the experimental flow rate. The results from (5) are compared to experimental data from thermocouples located at $x = 12$ cm and depth varying from $z = -2$ mm to $z = -12$ mm in the next section. The position of the topmost thermocouple is known with an uncertainty of ± 1.5 mm.

Though the Reynolds number computed in tab.3 is greater than 1, the comparison of the experimental position of the spreading front advance and self-similar solutions obtained from viscous-

gravity balance by Huppert [32] and Longo et al. [33] on fig. 6 shows good agreement. Based on this comparison, our physical model should properly represent the phenomena of the spreading, even though the inertia term is lacking.

5. Results and Discussion

Numerical simulations were performed to test the ability of a code developed by Bernabeu et al. [16] for lava flow to reproduce corium spreading experiments. We choose to use the physical parameters provided in the VEU7 benchmark [3] in order to be able to compare our results to those already existing.

In our model, the parameters Arr the Shaw law coefficient, n the fluid index and $\tau_{y,e}$ the yield stress are not given in the benchmark conducted by Journeau et al. [3] and few studies have been conducted on them for a Herschel-Bulkley behavior law for corium such as that of Roche et al. [11]. Thus we conduct a sensitivity analysis on them to determine the limits of our model on the spreading length evolution.

5.1. Sensitivity analysis

The coefficient Arr has an influence on the evolution of rheological properties of the fluid against temperature, and the characteristic time for heat diffusion is $t_{thermal} = \frac{H^2 \rho c_p}{k} = 7150\ s$, which two orders of magnitude greater than the flow time. Fig. 7 shows that for different values of this coefficient around those computed from the works of Roche et al. [11] and Ramacciotti et al. [18], it has almost no influence. We thus keep the value $Arr = 7.10^{-3}$ from Roche et al. [11] for the following simulations.

The fluid index n has a strong influence on both the slope of the spreading front evolution, its stopping time and final location as shown on fig. 8. According to this figure, the value of $n = 1$ corresponding to the Binghamian model yields a clearer asymptote, though the logarithmic representation fig. 9 shows better agreement in terms of slope for the value $n = 0.66$ before the end of the corium supply, excepted for the first experimental point that corresponds to a corium splash (experimental artefact in the VEU7 test). To keep a better agreement with experimental spreading dynamic, the latter value is used for further analysis.

According to fig. 10, values of $\tau_y = 50\ Pa$ and $\tau_y = 200\ Pa$ show the best agreement in terms of spreading dynamic, respectively for the spread on the ceramic and concrete substrates. The difference in the two values for the same experiment could be explained by the uncertainties on the symmetry of the experimental flow rate and a lack of a degassing model for the concrete substrate, that was observed by Journeau et al. [1]. Though the complete stop is not reached in these cases, the velocity of the front edge shown on fig. 11 decreases faster than exponentially, indicating an asymptote. This differs from newtonian models where the melt would spread infinitely for an infinite time, where a viscoplastic model gives a finite spread in a infinite time.

5.2. 3D Visualisation of velocity and temperature field

Using the two dimensional solution $(h, \overline{\theta})$ and the dimensionless equations yielded through the process of vertical averaging described in Bernabeu et al. [16], we compute and visualize the tridimensional velocity and temperature profiles, enabling faster computation. Fig. 12 shows the enlargement of the plug region defined by the plug height h_c above which the viscoplastic fluid behaves as a pseudo-solid, effectively having a rigid body movement. We also see a rise in height during supply of the melt, followed by a decrease due to spread from gravity effect.

5.3. Temperature field in the substrate

Using the solution by Carslaw and Jaeger (5), we compare the temperature evolution of the substrate in the simulation with that measured experimentally at the location $x = 12\ cm$ and various depths. The topmost thermocouple is located at $z = -2 \pm 1.5\ mm$, and as shown on fig.13, the simulation at the lower boundary of this interval is in good agreement with the experiment. The largest differences between simulation and experiment are found for temperatures above 100 ^oC, which can be partially explained by the gas release in the substrate. The temperature profiles presented in fig. 14 confirm that the first few millimeters of the substrate attain degassing temperature during the spreading. We can assume that molten core concrete interaction starts before the end of the spreading. Concrete ablation depth is estimated to be lesser than a millimeter at the time of spread stop, though we are overestimating substrate temperature since we are not modelling free water and CO_2 phase change here. This is in accordance with our lack of chemical reaction model in the spreading process.

5.4. Comparison to other nuclear accident spreading code

We compare the present model simulation with the CORFLOW [8, 34], LAVA [35] and THEMA [6] codes results provided in the VEU7 benchmark by Journeau et al. [3] on fig. 15. For the THEMA and CORFLOW codes as well as ours, using the same corium properties for the spreading on the different substrates yields similar dynamic and final spreading length. In LAVA, Journeau et al. [3] obtained different spreading length for both substrates by adding an extra heat loss term on concrete of the order of 500 kW/m^2 to take into account the gas sparging observed on this side.

Overall, all four codes provide satisfactory results in terms of spreading front evolution and final length. The use of the Herschel-Bulkley (1a) constitutive law enable us to provide closer results in terms of dynamics during the corium inlet feeding period and to add another potential explanation for the corium stoppage. Indeed, observations on the VEU7 experiment in [1] show that the formation of a crust happens after complete stop of the spreading, meaning that conditions on a stop temperature or solid fraction might not be enough to explain it.

6. Conclusions

Lava and corium flows have been compared and arguments for the modelling of the latter as a non-isothermal free-surface viscoplastic flow have been presented. Results on the spreading of corium using the model developed by Bernabeu et al. [16] have been compared to the VEU7 experiment [3]. Both the spreading length and temperature evolution in the susbtrate show encouraging agreement. Future work will use a more representative thermal distribution in the fluid height and gas release from the substrate. More experimental investigation on the material properties of corium, mainly its yield stress and fluid index are needed to improve its understanding under cooling conditions. Moreover, in other experiments, the effect of MCCI in the spreading process might be greater, necessitating chemical description in the model to take it into account. Improving the comprehension of these phenomena would give greater insight on corium spreading in the scope of the EVR strategy.

References

References

[1] C. Journeau, E. Boccaccio, C. Brayer, G. Cognet, J.-F. Haquet, C. Jégou, P. Piluso, J. Monerris, Ex-vessel corium spreading: results from the VULCANO spreading tests, Nuclear Engineering and Design 223 (1) (2003) 75–102. doi:10.1016/S0029-5493(02)00397-7.
URL https://linkinghub.elsevier.com/retrieve/pii/S0029549302003977

[2] H. Weisshäupl, Severe accident mitigation concept of the EPR, Nuclear Engineering and Design 187 (1) (1999) 35–45. doi:10.1016/S0029-5493(98)00256-8.
URL https://linkinghub.elsevier.com/retrieve/pii/S0029549398002568

[3] C. Journeau, J.-F. Haquet, B. Spindler, C. Spengler, J. Foit, The VULCANO VE-U7 Corium spreading benchmark, Progress in Nuclear Energy 48 (3) (2006) 215–234. doi:10.1016/j.pnucene.2005.09.009.
URL https://linkinghub.elsevier.com/retrieve/pii/S0149197005001782

[4] M. Johnson, A. Denoix, V. Bouyer, H. Goda, S. Kamohara, J. Takeuchi, L. Brissonneau, C. Journeau, High-temperature ex-vessel corium spreading. Part 1: experimental investigations on ceramic and sacrificial concrete substrates, Journal of Nuclear Science and Technology (2021) 1–13doi:10.1080/00223131.2021.1977199.

[5] M. Johnson, T. Schiano, A. Denoix, V. Bouyer, C. Journeau, High-temperature ex-vessel corium spreading. Part 2: scaling principles for gravity-viscous spreading with slip at the melt–substrate interface, Journal of Nuclear Science and Technology (2021) 1–13doi:10.1080/00223131.2021.1978895.

[6] B. Spindler, J. M. Veteau, The simulation of melt spreading with THEMA code Part 1: Model, assessment strategy and assessment against analytical and numerical solutions, Nuclear Engineering and Design (2006) 10doi:10.1016/j.nucengdes.2005.09.009.

[7] M. T. Farmer, the meltspread code for modeling of ex-vessel core debris spreading behavior, Tech. Rep. ANL-18/30, argonne national lab., usa, https://www.osti.gov/biblio/1483992 (2018).
URL https://www.osti.gov/biblio/1483992

[8] R. Wittmaack, Simulation of Free-Surface Flows with Heat Transfer and Phase Transitions and Application to Corium Spreading in the EPR, Nuclear Technology 137 (3) (2002) 194–212. doi:10.13182/NT02-A3268.
URL https://www.tandfonline.com/doi/full/10.13182/NT02-A3268

[9] K. R. Robb, M. Farmer, M. W. Francis, Ex-Vessel Core Melt Modeling Comparison between MELTSPREAD-CORQUENCH and MELCOR 2.1, Tech. Rep. ORNL/TM–2014/1, 1185398 (Mar. 2014). doi:10.2172/1185398.
URL http://www.osti.gov/servlets/purl/1185398/

[10] A. Yamaji, X. Li, Development of MPS Method for Analyzing Melt Spreading Behavior and MCCI in Severe Accidents, Journal of Physics: Conference Series 739 (2016) 012002. doi:10.1088/1742-6596/739/1/012002.
URL https://iopscience.iop.org/article/10.1088/1742-6596/739/1/012002

[11] M. Roche, D. Steidl, L. Leibowitz, J. Fink, B. Raj Sehgal, Viscosity of corium-concrete mixtures at high temperatures., Argonne National Laboratory Report ACE-TR-C37, Argonne National Laboratory, ANL (1994).

[12] W. H. Herschel, T. Bulkley, Measurement of consistency as applied to rubber-benzene solutions, Proc. Amer. Soc. Testing Material 26 (2) (1926) 621–633.

[13] E. C. Bingham, Fluidity and plasticity, Mc Graw-Hill, New-York, USA, 1922, http://www.archive.org/download/fluidityandplast007721mbp/fluidityandplast007721mbp.pdf.

[14] P. Saramito, A. Wachs, Progress in numerical simulation of yield stress fluid flows, Rheologica Acta 56 (3) (2017) 211–230. doi:10.1007/s00397-016-0985-9.
URL http://link.springer.com/10.1007/s00397-016-0985-9

[15] N. Bernabeu, P. Saramito, C. Smutek, Numerical modeling of non-Newtonian viscoplastic flows: part II. Viscoplastic fluids and general tridimensional topographies, Int. J. Numer. Anal. Model. 11 (1) (2014) 213–228.

[16] N. Bernabeu, P. Saramito, C. Smutek, Modelling lava flow advance using a shallow-depth approximation for three-dimensional cooling of viscoplastic flows, Geological Society, London, Special Publications 426 (1) (2016) 409–423. doi:10.1144/SP426.27.
URL http://sp.lyellcollection.org/lookup/doi/10.1144/SP426.27

[17] H. R. Shaw, Rheology of Basalt in the Melting Range, Journal of Petrology 10 (3) (1969) 510–535. doi:10.1093/petrology/10.3.510.
URL https://academic.oup.com/petrology/article-lookup/doi/10.1093/petrology/10.3.510

[18] M. Ramacciotti, C. Journeau, F. Sudreau, G. Cognet, Viscosity models for corium melts, Nuclear Engineering and Design 204 (1-3) (2001) 377–389. doi:10.1016/S0029-5493(00)00328-9.
URL https://linkinghub.elsevier.com/retrieve/pii/S0029549300003289

[19] N. Roquet, P. Saramito, An adaptive finite element method for Bingham fluid flows around a cylinder, Computer Methods in Applied Mechanics and Engineering 192 (31-32) (2003) 3317–3341. doi:10.1016/S0045-7825(03)00262-7.
URL https://linkinghub.elsevier.com/retrieve/pii/S0045782503002627

[20] P. Saramito, Rheolef 7.1, an efficient C++ finite element environment (2019).
URL https://www-ljk.imag.fr/membres/Pierre.Saramito/rheolef/html/index.html

[21] F. Hecht, BAMG: bidimensional anisotropic mesh generator, https://www.ljll.math.upmc.fr/hecht/ftp/bamg (2006).

[22] H. S. Carslaw, J. C. Jaeger, Conduction of heat in solids, Oxford university press, 1959.

[23] N. Villeneuve, D. R. Neuville, P. Boivin, P. Bachèlery, P. Richet, Magma crystallization and viscosity: A study of molten basalts from the Piton de la Fournaise volcano (La Réunion island), Chemical Geology 256 (3-4) (2008) 242–251. doi:10.1016/j.chemgeo.2008.06.039.
URL https://linkinghub.elsevier.com/retrieve/pii/S0009254108002635

[24] A. R. McBirney, T. Murase, Rheological Properties of Magmas, Annual Review of Earth and Planetary Sciences 12 (1) (1984) 337–357. doi:10.1146/annurev.ea.12.050184.002005.
URL http://www.annualreviews.org/doi/10.1146/annurev.ea.12.050184.002005

[25] H. Pinkerton, G. Norton, Rheological properties of basaltic lavas at sub-liquidus temperatures: laboratory and field measurements on lavas from Mount Etna, Journal of Volcanology and Geothermal Research 68 (4) (1995) 307–323. doi:10.1016/0377-0273(95)00018-7.
URL https://linkinghub.elsevier.com/retrieve/pii/0377027395000187

[26] J. Durand, P. Tulet, M. Leriche, S. Bielli, N. Villeneuve, A. D. Muro, J.-B. Fillipi, Modeling the lava heat flux during severe effusive volcanic eruption: An important impact on surface air quality: DURAND ET AL., Journal of Geophysical Research: Atmospheres 119 (20) (2014) 11,729–11,742. doi:10.1002/2014JD022034.
URL http://doi.wiley.com/10.1002/2014JD022034

[27] C. Journeau, F. Sudreau, J.-M. Gatt, G. Cognet, Thermal, physico-chemical and rheological boundary layers in multi-component oxidic melt spreads, International Journal of Thermal Sciences 38 (10) (1999) 879–891. doi:10.1016/S1290-0729(99)80042-8.
URL https://linkinghub.elsevier.com/retrieve/pii/S1290072999800428

[28] F. Sudreau, G. Cognet, Corium viscosity modelling above liquidus temperature, Nuclear Engineering and Design 178 (3) (1997) 269–277. doi:10.1016/S0029-5493(97)00137-4.
URL https://linkinghub.elsevier.com/retrieve/pii/S0029549397001374

[29] P. Piluso, J. Monerris, C. Journeau, G. Cognet, Viscosity measurements of ceramic oxides by aerodynamic levitation, Int. J. Thermophys. 23 (5) (2002) 1229–1240.

[30] C. Ancey, H. Jorrot, Yield stress for particle suspensions within a clay dispersion, Journal of Rheology 45 (2) (2001) 297–319. doi:10.1122/1.1343879.
URL http://sor.scitation.org/doi/10.1122/1.1343879

[31] G. Cognet, H. Alsmeyer, W. Tromm, D. Magallon, R. Wittmaack, B. R. Sehgal, W. Widmann, L. D. Cecco, R. Ocelli, G. Azarian, D. Pineau, B. Spindler, G. Fieg, H. Werle, C. Journeau, M. Cranga, G. Laffont, Corium spreading and coolability CSC Project, Nuclear Engineering and Design (2001) 12doi:10.1016/S0029-5493(01)00395-8.

[32] H. E. Huppert, The propagation of two-dimensional and axisymmetric viscous gravity currents over a rigid horizontal surface, Journal of Fluid Mechanics 121 (-1) (1982) 43. doi:10.1017/S0022112082001797.

[33] S. Longo, V. Di Federico, L. Chiapponi, Propagation of viscous gravity currents inside confining boundaries: the effects of fluid rheology and channel geometry, Proceedings of the Royal Society A: Mathematical, Physical and Engineering Sciences 471 (2178) (2015) 20150070. doi:10.1098/rspa.2015.0070.

[34] R. Wittmaack, Corflow: A code for the numerical simulation of free-surface flow, Nuclear Technology 119 (2) (1997) 158–180. arXiv:https://doi.org/10.13182/NT97-A35384, doi:10.13182/NT97-A35384.
URL https://doi.org/10.13182/NT97-A35384

[35] H.-J. Allelein, A. Breest, C. Spengler, Simulation of core melt spreading with lava: theoretical background and status of validation, in: Proceedings of the OECD workshop on ex-vessel debris coolability, Karlsruhe (Germany), 2000.

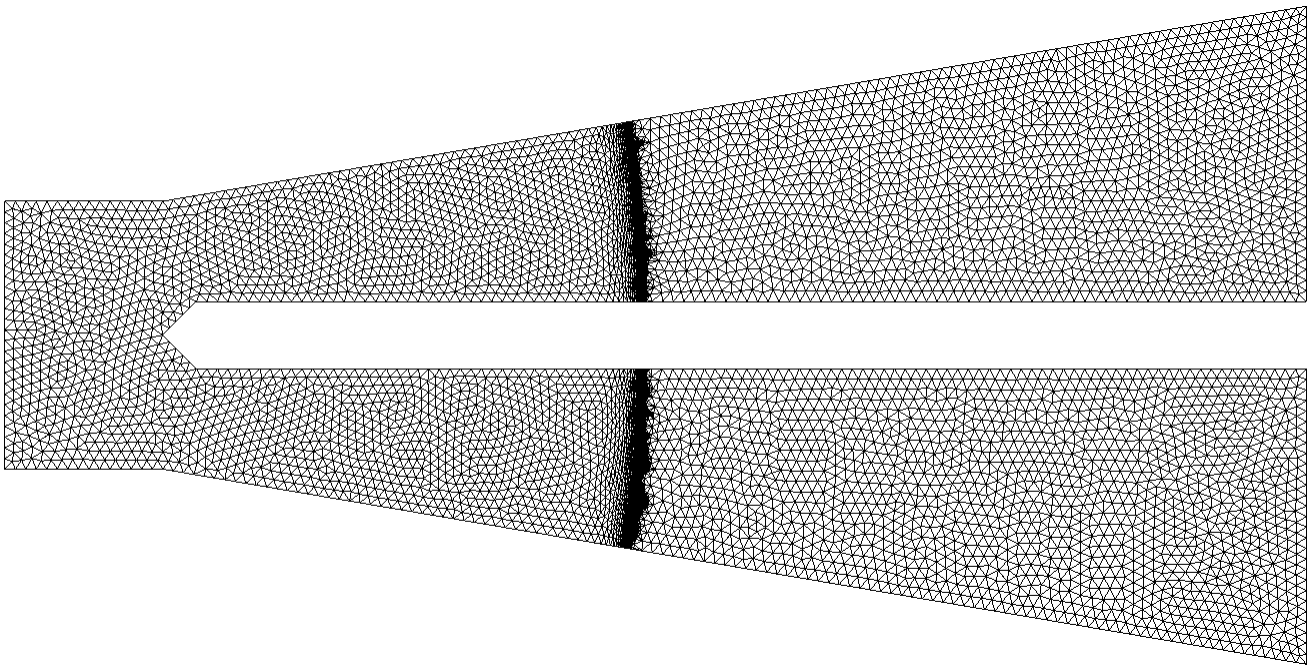

(a)

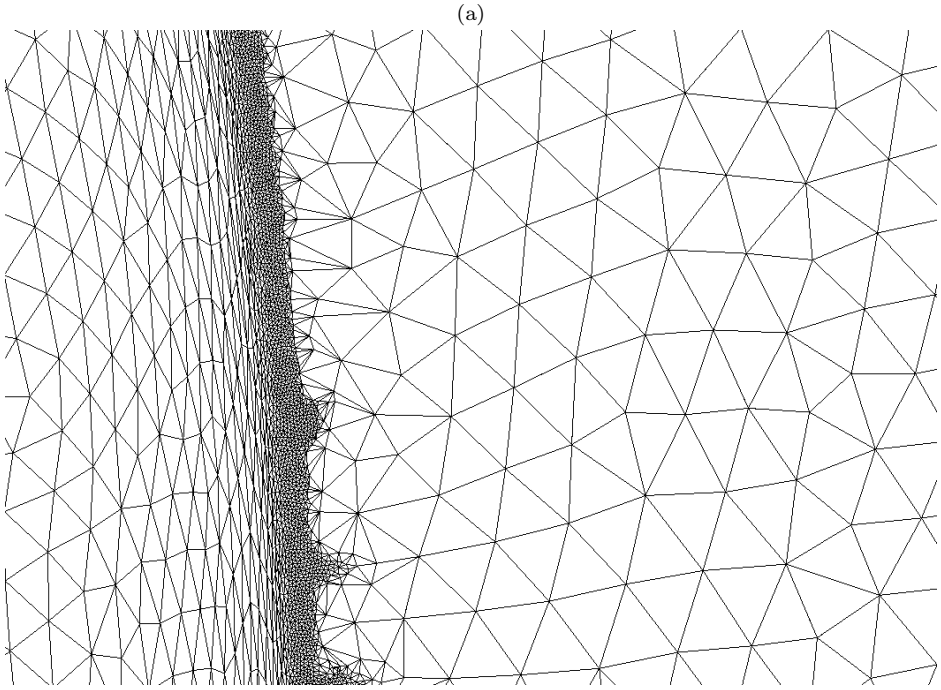

(b)

Figure 3: (a) Auto-generated mesh and (b) Zoom of mesh (a) at the front of the spread.

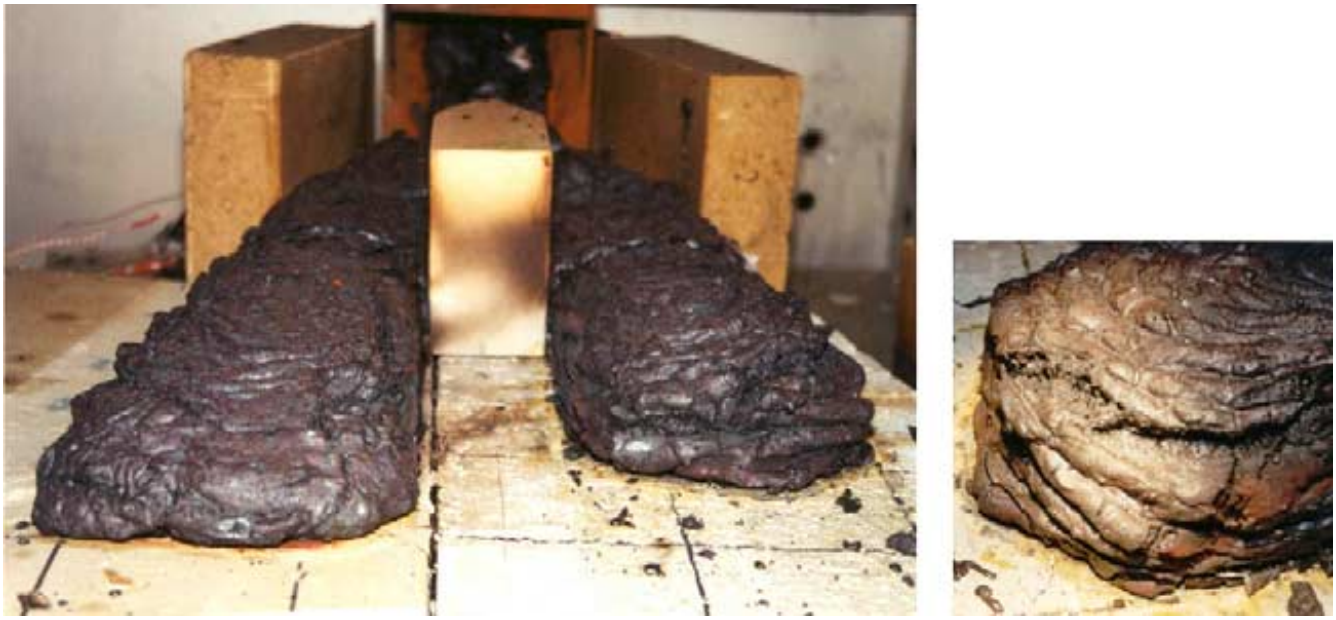

Figure 4: Post-mortem view of the VEU7 test, from Journeau et al. [3]

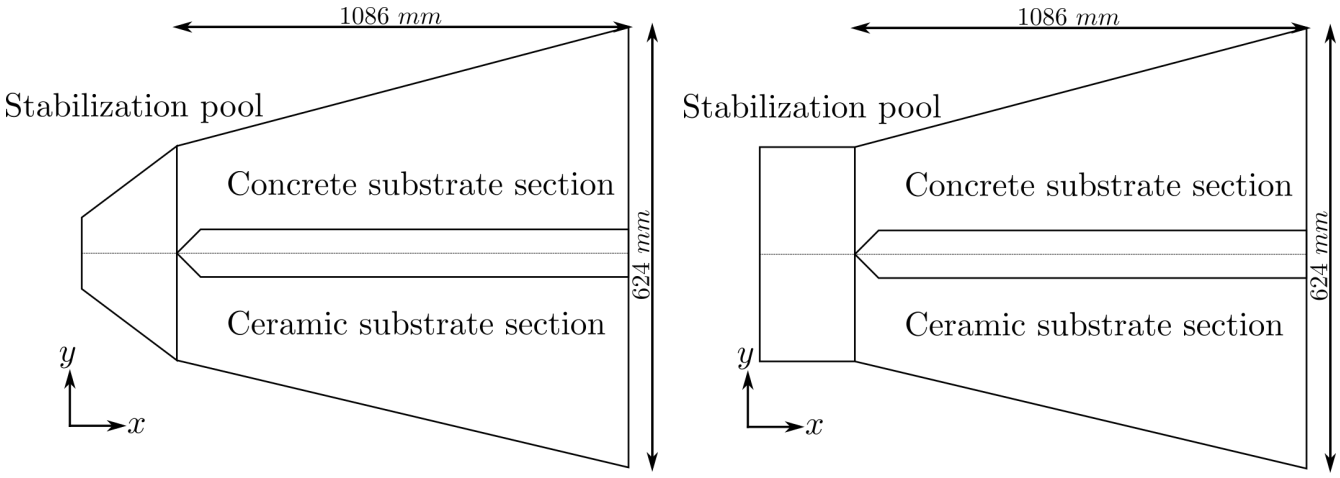

(a) (b)

Figure 5: (a) VEU7 spreading test diagram and (b) geometry used for simulations

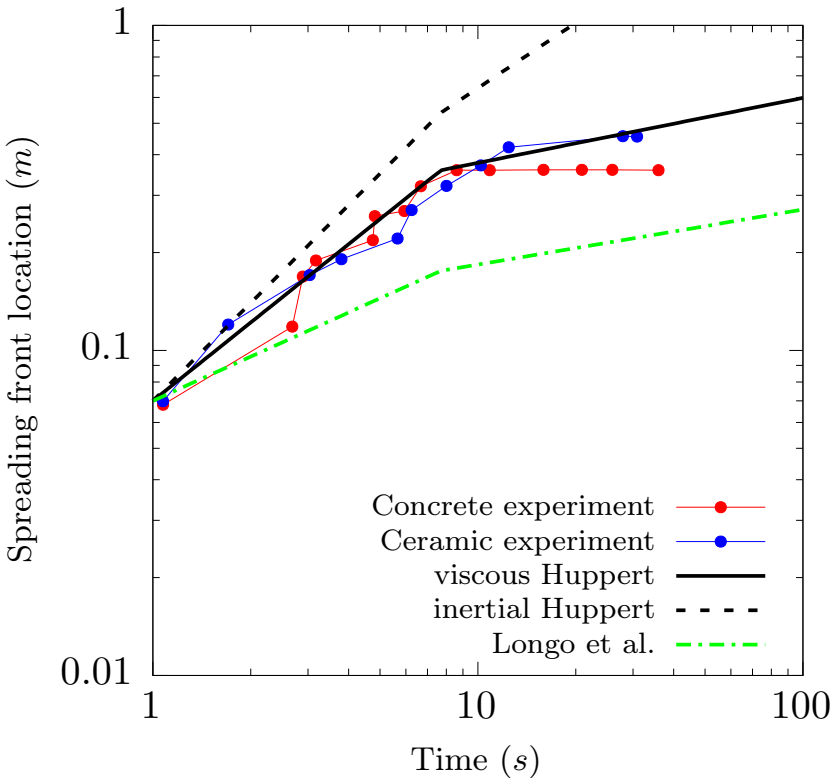

Figure 6: Experimental front position evolution and its comparison to self-similar solutions from [32, 33] for various geometries. We assume from this comparison that the process of corium spreading is mainly viscous during corium inlet feeding.

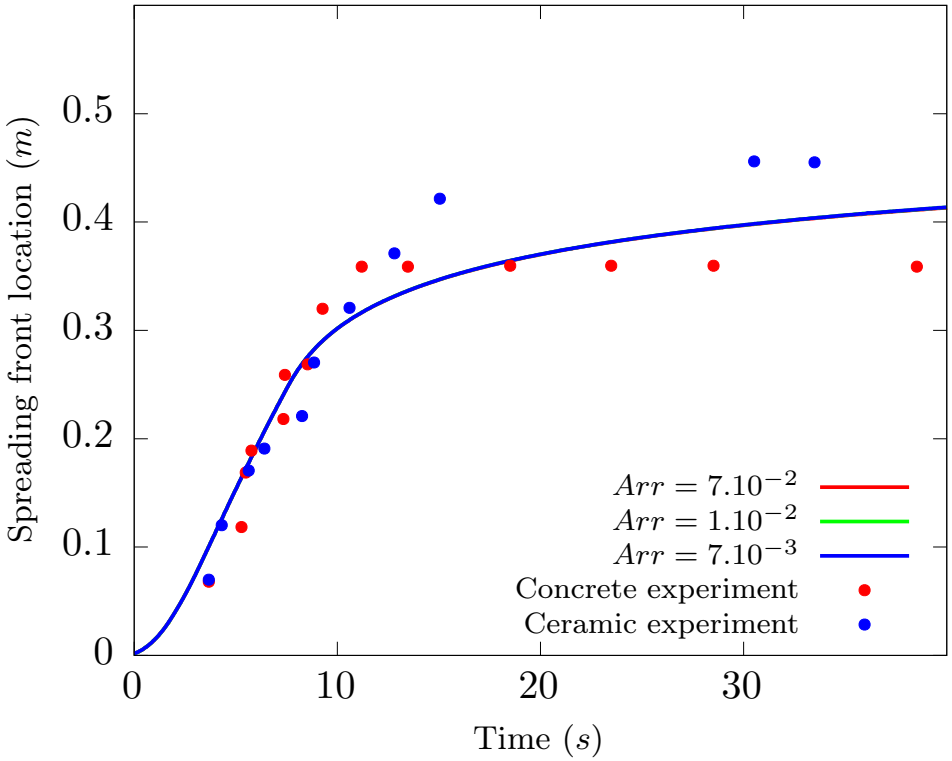

Figure 7: Simulated front progress for $n = 1$, $\tau_y = 100\ Pa$ and different values of the Shaw model coefficient Arr, and experimental results for the VEU7 test, for both concrete and ceramic substrate channels.

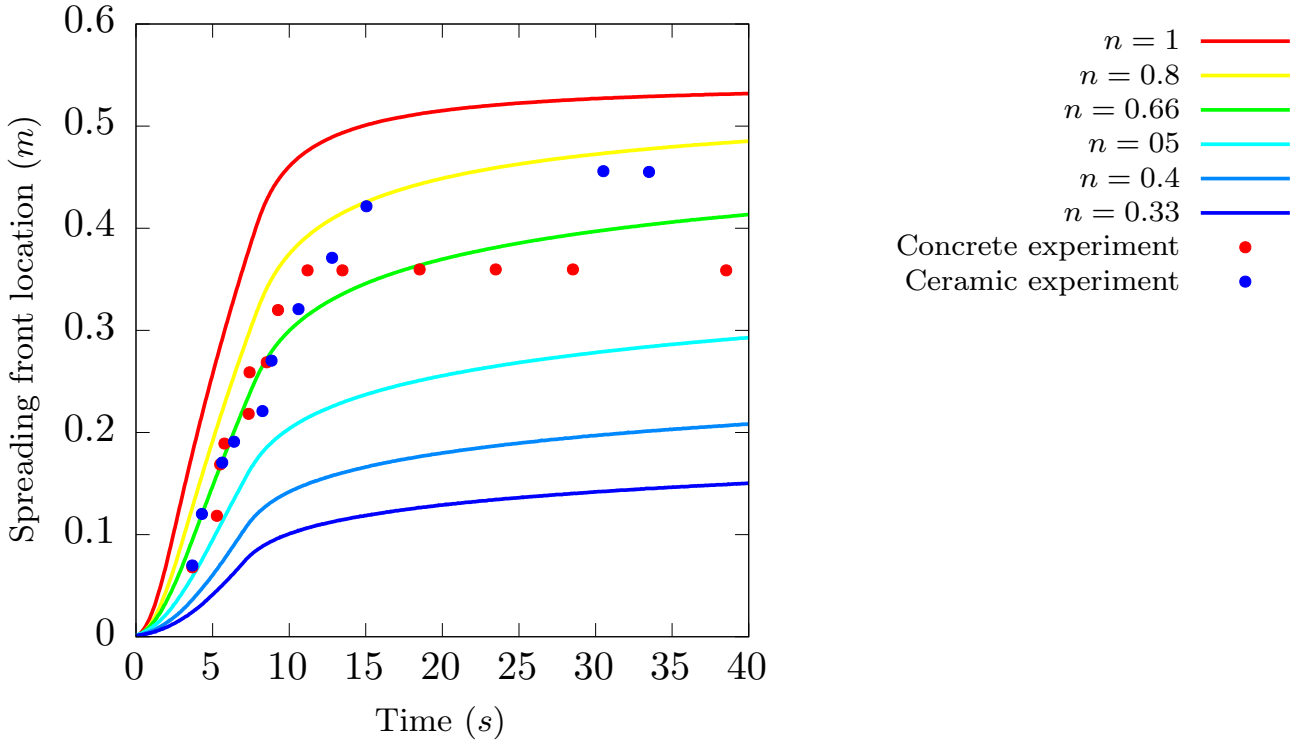

Figure 8: Simulated front progress for $Arr = 7.10^{-3}$, $\tau_y = 100\ Pa$ and different values of the fluid index n, and experimental results for the VEU7 test, for both concrete and ceramic substrate channels.

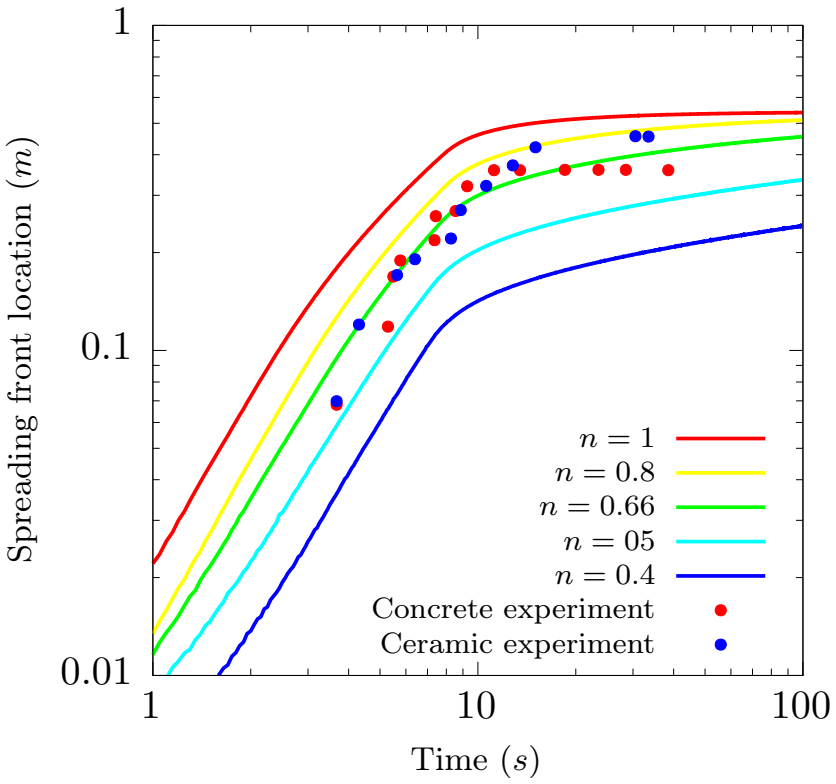

Figure 9: Simulated front progress for $Arr = 7.10^{-3}$, $\tau_y = 100\ Pa$ and different values of the fluid index n, and experimental results for the VEU7 test, for both concrete and ceramic substrate channels. log-log representation of fig. 8

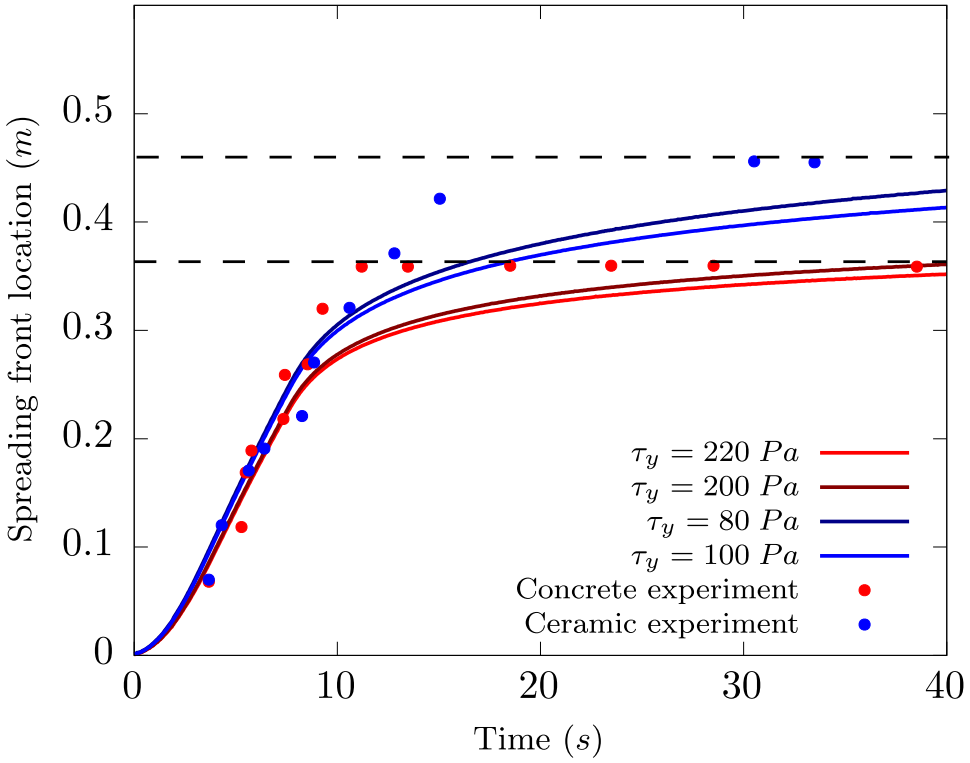

Figure 10: Simulated front progress for $n = 0.66$, $Arr = 7.10^{-3}$ and different values of the initial yield stress τ_y, and experimental results for the VEU7 test, for both concrete and ceramic substrate channels.

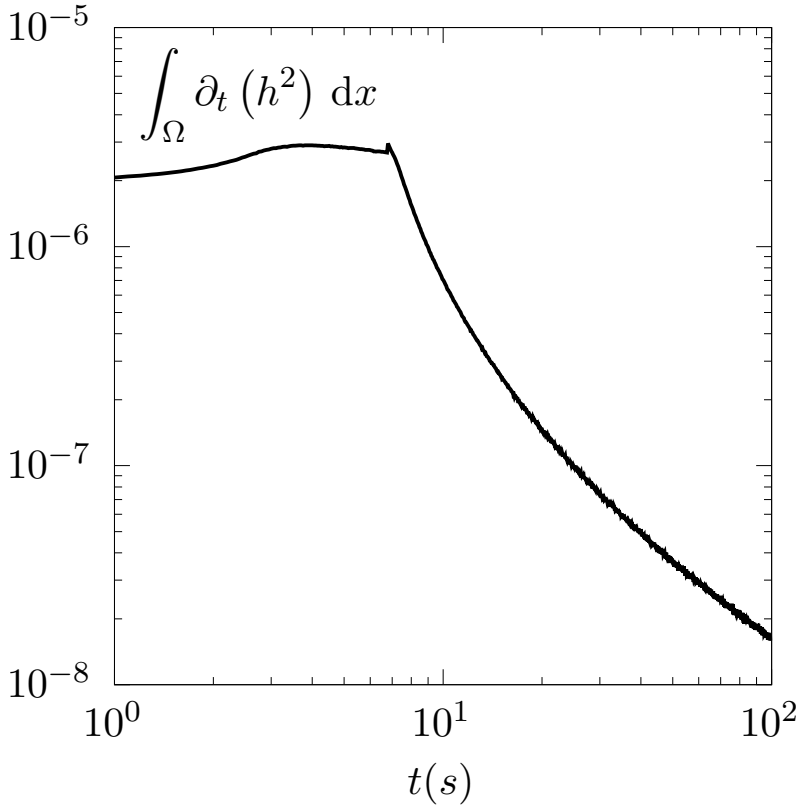

Figure 11: Evolution of $\int_\Omega (h^2) dx$, for the simulation with $n = 0.66$ and $\tau_y = 200\ Pa$. It shows that the movement of the melt slows down quickly once corium source stops at $t = 7.7s$.

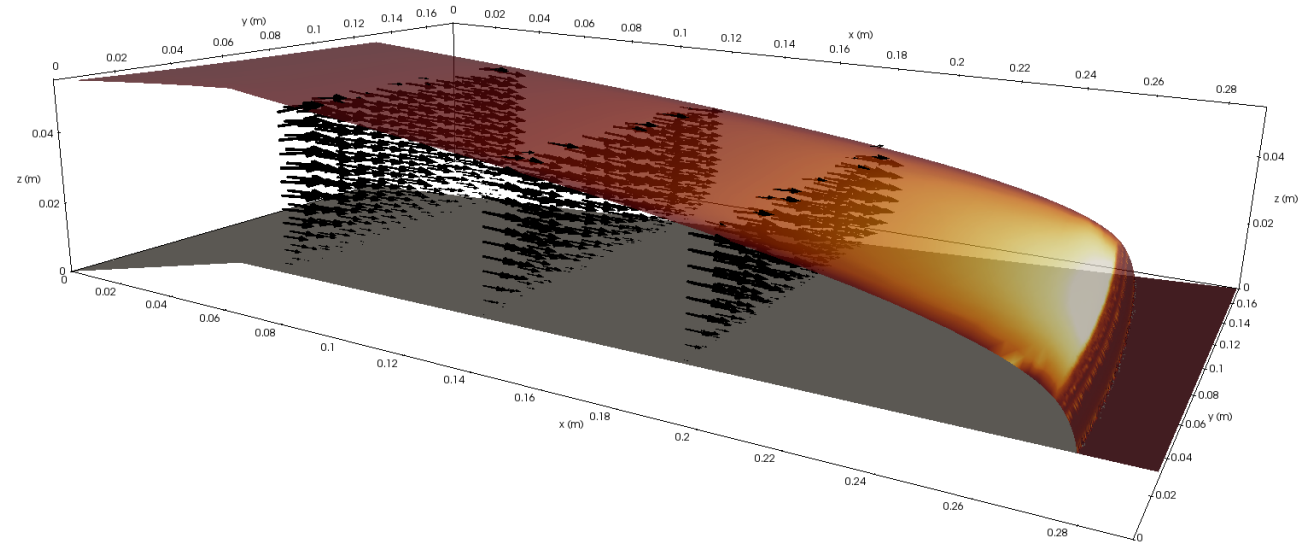

(a)

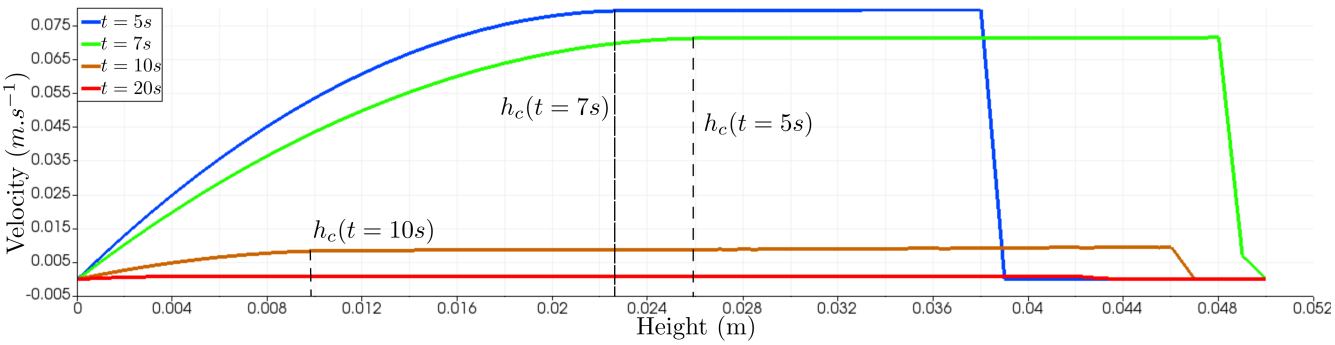

(b)

Figure 12: (a) Tridimensional reconstruction of the velocity. The top surface color represents height-averaged temperature. (b) Velocity profiles along the z-axis at $t = 5\ s$ (during melt supplying), $t = 7\ s$ (close to the end of melt supplying), $t = 10\ s$ (after the end of melt supply, toward melt front stop) and $t = 20\ s$ at $x = 12\ cm$ and $y = 10\ cm$

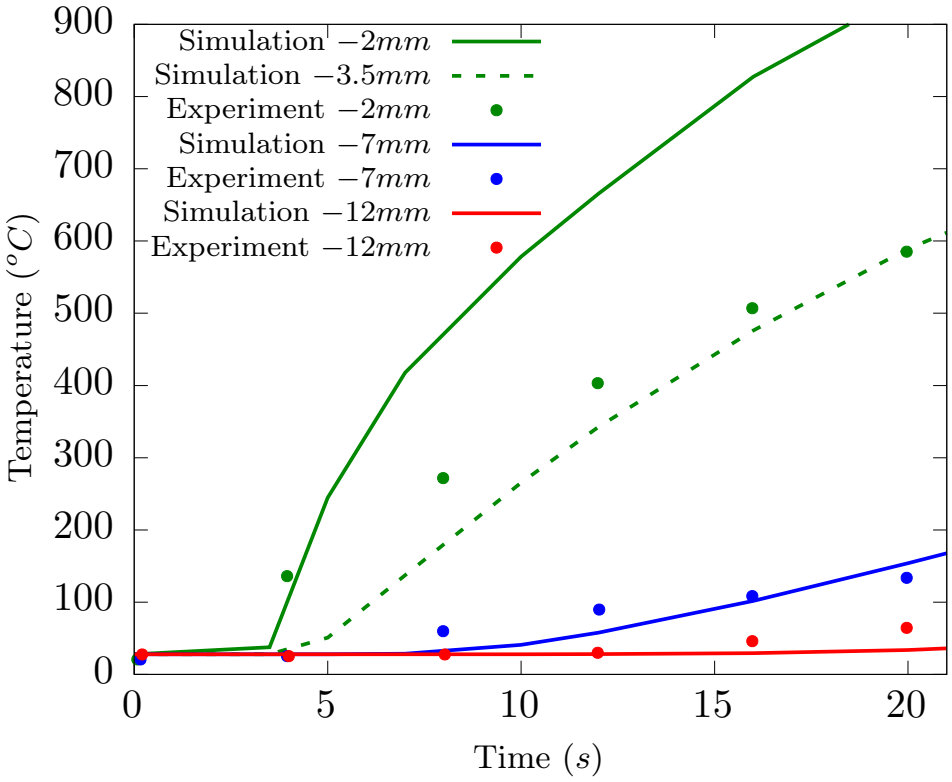

Figure 13: Concrete substrate temperature evolution for the VEU7 experiment and its simulation, for thermocouples at $x = 12\ cm$, $y = 10\ cm$ and $z = -2, -7, -12\ mm$.

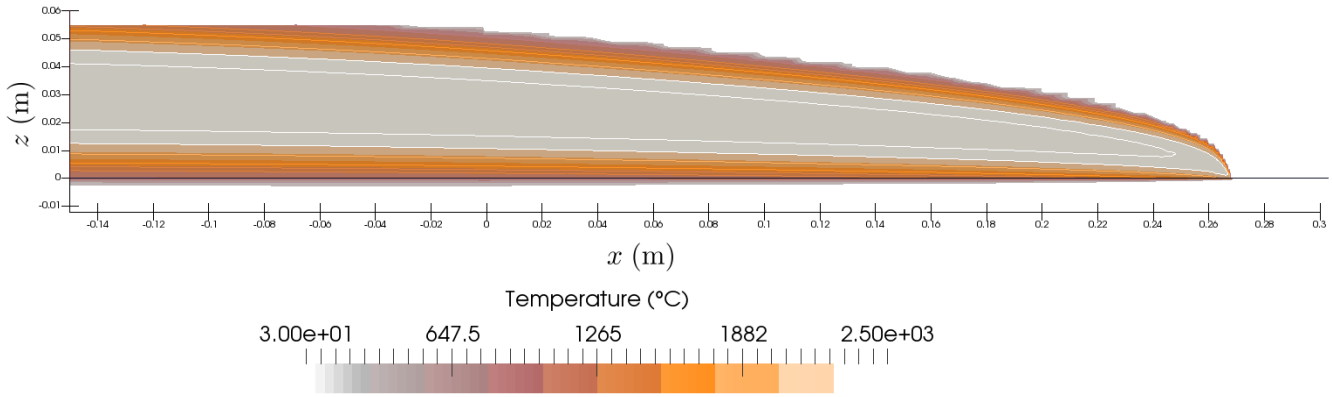

(a)

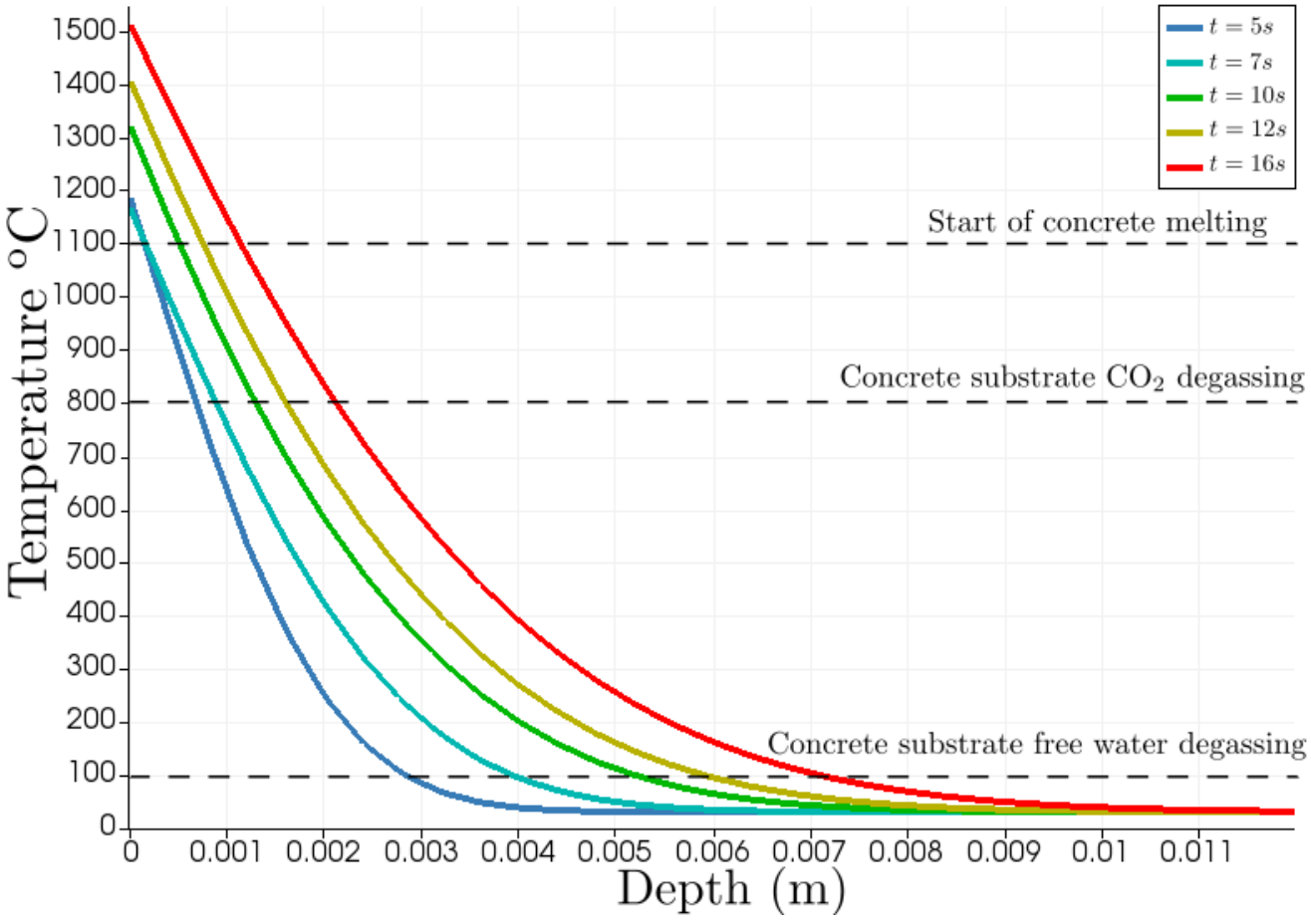

(b)

Figure 14: (a) Temperature at $y = 10\ cm$ and $t = 5s$, in both the melt and the substrate. (b) Concrete substrate temperature evolution for the VEU7 experiment and its simulation, for thermocouples at $x = 12\ cm$ and $y = 10\ cm$.

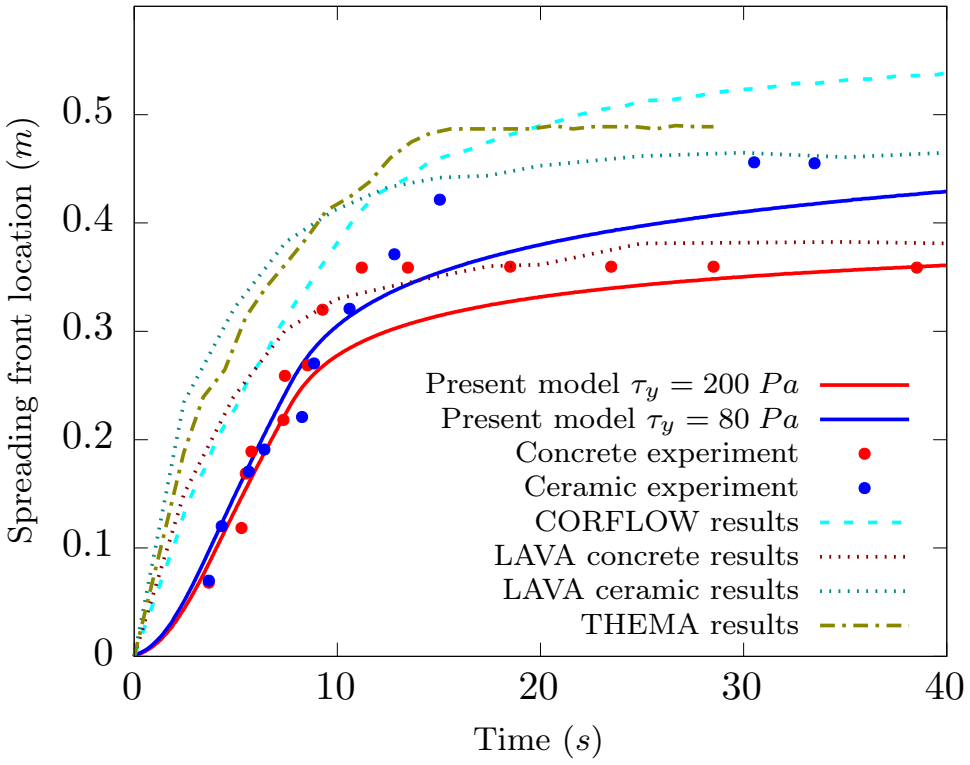

Figure 15: Comparison between the LAVA, CORFLOW, THEMA codes and the present model